IAEA nuclear fusion

Summary of reports presented to magnetic confinement theory and modelling (TH) section: main ideas and achievements

To cite this article: Yu.N. Dnestrovskij 2009 *Nucl. Fusion* **49** 104003

Nucl. Fusion **49** (2009) 104003 (14pp) doi:10.1088/0029-5515/49/10/104003

Summary of reports presented to magnetic confinement theory and modelling (TH) section: main ideas and achievements

Yu.N. Dnestrovskij

Institute of Nuclear Fusion, Russian Research Centre 'Kurchatov Institute', Moscow, Russian Federation

E-mail: dnyn@nfi.kiae.ru

Received 10 December 2008, accepted for publication 8 June 2009
Published 9 September 2009
Online at stacks.iop.org/NF/49/104003

Abstract
This is a summary of the reports presented to the 22nd IAEA Fusion Energy Conference, Magnetic confinement theory and modelling section (Geneva, October 2008). Many of the papers are devoted to the investigation of transport processes, in particular to the toroidal momentum transport. Simulation by gyrokinetic codes has been improved in many countries, and the number of available codes reaches several tens. Numerical developments tend to follow the same trend as improvements in the computation power. The timescale for plasma simulations is now comparable to the ion–ion collision time. To improve the predictions for ITER, the near future advances are the combination of gyrokinetic and fluid codes. Reports on stellarators confirm that in these devices the neoclassical transport dominates, but the influence of turbulent transport can play a role in improved confinement regimes and in the resilience of pressure profiles. The resonant magnetic perturbations, mitigating the ELMs, could brake the plasma rotation, increasing the danger of disruption. The problems on the scrape-off layer and the divertor attract a large number of theoretical works that could lead to a better understanding of periphery plasma processes. ITER and reactor studies have been presented, and calculations confirm that ITER can achieve $Q = 10$ or larger. It has also been shown that the alpha-particle diffusion due to drift driven ITG turbulence will be relatively small in ITER, uncertainty remains in the magnitude of alpha-particle diffusion due to Alfvén waves.

PACS numbers: 52.35.−g, 52.50.−b, 52.65.−y, 52.65.Tt

(Some figures in this article are in colour only in the electronic version)

1. Introduction

This is a summary of the advances in the magnetic fusion theory research presented at the 22nd IAEA Fusion Energy Conference from 13 to 18 October 2008 in Geneva, Switzerland. Table 1 shows the total number of reports and their distribution along different primary scientific themes. As most reports spanned multiple scientific themes, reports have been catalogued only by primary scientific theme. The main goal of the research was the ability to predict fusion performance with great reliability. It is impossible in this short review to consider all the presented reports, so we are limiting ourselves to the most interesting ones from the point of view of new ideas and achievements.

2. Transport, gyrokinetics, turbulence

Research on transport processes and toroidal momentum transport attracted the most attention in this Conference. Quasi-linear fluid models and gyrokinetic simulation described many features of the experimental data.

2.1. Quasi-linear fluid models

Several reports are devoted to the new developments and applications of quasi-linear fluid models. Staebler *et al* report on the creation of a new transport code TGLF (Trapped Gyro-Landau Fluid) [1]. This is a development of the well-known widely used code GLF23. Figure 1 shows the verification

Table 1. Distribution of reports among different topics.

Topic	Number of reports
Transport, gyrokinetics, turbulence	54
Waves and instabilities	31
SOL and divertor	17
ITER and reactors	11
Stellarators and other helical configurations	9
Fast particles	6
Total number of TH reports	128

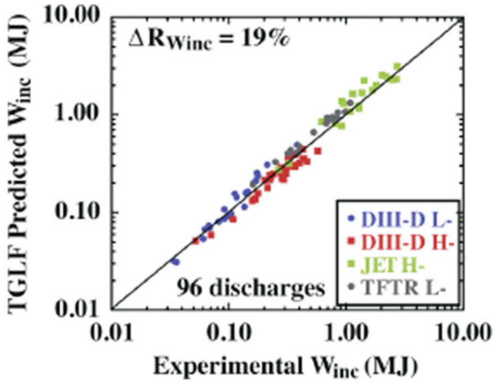

Figure 1. Incremental stored energy $W_{\rm inc} = W - W_{\rm boundary}$ predicted by TGLF versus experimental data from 96 tokamak discharges.

of this new code by the comparison of the calculated values of the incremental stored energy $W_{\rm inc}$ with experimental data from DIII-D, JET and TFTR tokamaks for L- and H-modes. It is seen that such global values as the energy storage are reproduced well by this code. However, the problem of plasma periphery description in the region $\rho > 0.8$ is not solved in the new code as in the previous one. The boundary conditions have to be formulated at the point $\rho = 0.8$, so additional periphery information from experiment is needed.

Bourdelle *et al* present a new quasi-linear code called QuaLiKiz [2]. The code was verified by comparison with the results obtained by the non-linear gyrokinetic code GYRO using ITG and TEM turbulence. QuaLiKiz is working much faster than GYRO. Quasi-linear fluxes are compared with the fluxes calculated by the GYRO code (figure 2). The resulting quasi-linear flux is shown to agree with the non-linear one when varying the ion to electron temperature ratio from the ITG to the TEM mode. Lin *et al* discuss the foundation of the quasi-linear models by the gyrokinetic code [3]. For this, the gyrokinetic turbulence simulations with the GTC code were provided to verify the validity of the quasi-linear theory (QLT). This validity depends on the ordering of several characteristic timescales of the turbulence. In particular, the Chirikov stochasticity parameter $S > 1$ and the turbulence Kubo number $K > 1$ are required for the validity of the QLT. The results of validation are different for different kinds of turbulence. For the ETG turbulence, it is shown that the stochastic parallel wave–particle decorrelation is the dominant mechanism responsible for electron heat transport driven by the ETG turbulence. The kinetic timescale of the wave–particle decorrelation is much shorter than the fluid timescale of the eddy mixing, so the kinetic Kubo number $K < 1$. Consistently, the transport is proportional to the

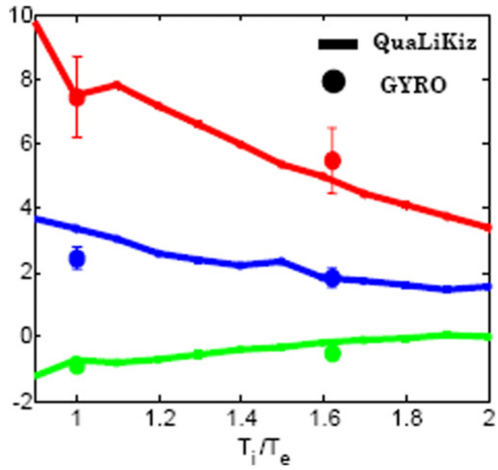

Figure 2. Quasi-linear fluxes (solid lines) normalized to one single non-linear ion heat flux, versus $T_{\rm i}/T_{\rm e}$. Red (upper curve): ion heat flux; blue (middle curve): electron heat flux; green (lower curve): particle flux. Points correspond to GYRO calculations.

local fluctuation intensity, and quasi-linear calculation of the electron heat conductivity agrees well with the simulation. For the ITG turbulence, the ion transport is regulated by the wave–particle decorrelation. The electron thermal transport is driven by non-resonant interactions. As a result, both the particle transport and the electron heat transport are much smaller than the ion thermal transport. The CTEM (collisionless trapped electron mode) instability is typically dominated by the precessional resonance of trapped electrons. The detuning of this resonance is much weaker than in the ITG and ETG turbulence. The simulation by the GTC code indicates that this detuning and mixing timescales in the CTEM turbulence are comparable rendering the applicability of the quasi-linear methods somewhat problematic.

Holand *et al* consider the combination of gyrokinetic and quasi-linear codes [4]. Using the new TGYRO transport code, which adjusts local plasma scale lengths within a GYRO simulation, it is possible to compare the temperature profiles at each time step. Using local, fixed-gradient simulations, GYRO is able to simultaneously reproduce ion and electron energy flows calculated via the ONETWO code (figure 3). Inside $\rho < 0.5$ GYRO matches ONETWO results, while in the plasma edge at $\rho = 0.75$ GYRO underestimates energy flows by a factor of 7 and RMS fluctuation levels by a factor of 3.

Idomura *et al* show the results of the attempts to increase the time duration of gyrokinetic calculations using a novel non-dissipative, conservative finite-difference scheme, which guarantees numerical stability by satisfying the relevant conservation properties of the gyrokinetic theory [5]. The ITG turbulence simulations are performed using a global gyrokinetic full-f Vlasov code GT5D, which is extended including a linear Fokker–Planck collision operator. In a normal shear tokamak with $\nu^* \sim 0.1$ and $(\rho^*)^{-1} \sim 150$, profile evolutions are traced over an ion collision time using a source and a sink, which fix the input power near the axis and the ion temperature at the edge, respectively. It is found that the turbulent transport due to quasi-periodic avalanches is dominant in source free regions, which are characterized

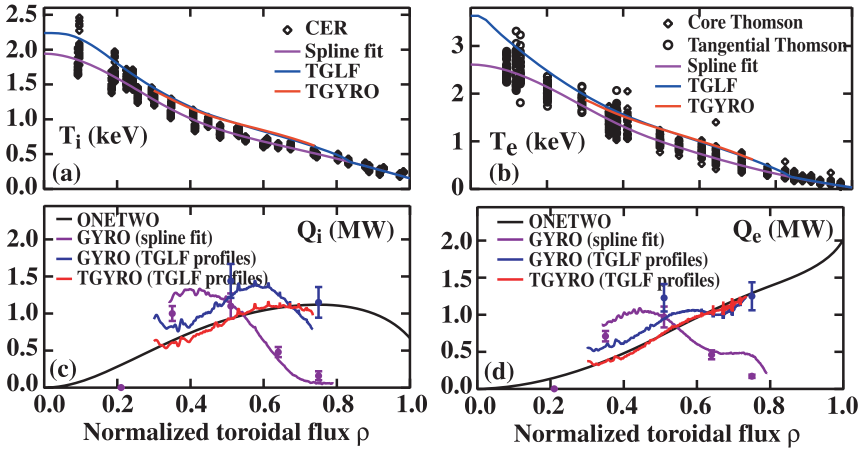

Figure 3. Equilibrium T_{i} (*a*) and T_{e} (*b*) profiles calculated as spline fits (purple) to the measured data (black points), as well as the TGLF flow-matching profiles (blue) and TGYRO adjustments to those profiles (red). The corresponding energy flows are shown in (*c*) and (*d*). ONETWO calculations using the spline fits are shown in black, GYRO results using the spline fits in purple (global results as solid lines and local results as individual points), GYRO results using the TGLF profiles in blue and TGYRO results starting from the TGLF profiles in red.

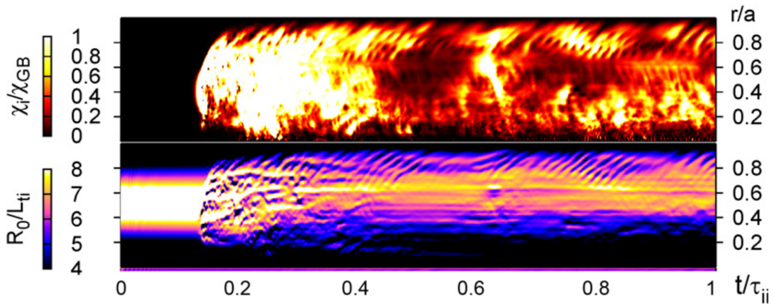

Figure 4. Spatio-temporal ($0 < t/\tau_{\mathrm{ii}} < 1$) contour plots of the normalized ion heat diffusivity χ_i and normalized temperature gradient $R/L_{T_{\mathrm{i}}}$, observed in a ITG turbulence simulation using GT5D.

by globally constant gradient length $L_{T_{\mathrm{i}}}$ near a critical value on average, and shows stiffness with increasing input power. Avalanches are affected by the radial electric field E_r, which is determined self-consistently by a momentum balance in the presence of neoclassical viscosity and turbulence, and they propagate outwards (inwards) with $\mathrm{d}E_r/\mathrm{d}r > 0$ ($\mathrm{d}E_r/\mathrm{d}r < 0$). E_r shear also affects the momentum transport leading to the sustainment of non-zero (intrinsic) toroidal rotation without momentum input near the axis. Figure 4 illustrates the radial-time distribution of the normalized ion heat diffusivity and ion temperature gradient. It is seen that the characteristic time of avalanches is approximately two orders of value less than the ion collision time τ_{ii}. In the conditions of the JT-60U device, $\tau_{\mathrm{ii}} \sim 20$ ms, so the period of avalanches is ~0.2 ms.

Jenko *et al* report about the development of the gyrokinetic non-linear GENE code [6]. Gyrokinetic simulations of micro-turbulence simultaneously driven by ETG, TEM and ITG modes are presented. In particular, it is found that different microinstabilities (such as ITG modes and TEMs) can interfere destructively, exhibiting significant deviations from the conventional simple predictions, but better agreement between simulations and experiments. Figure 5 shows as an example the calculated turbulence spectrum. The peaks related to ion and electron modes are clearly seen.

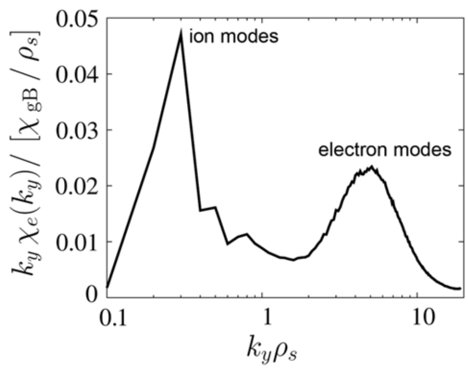

Figure 5. Turbulence spectrum at the simultaneous inclusion of the ion and electron modes in the gyrokinetic calculations.

2.2. *Momentum transport*

As discussed by Diamond *et al* [7], various mechanisms were proposed to describe turbulent momentum transport and the origin of spontaneous rotation. Several authors now accept that the flux $\pi_{r,\varphi}$ of toroidal momentum U_φ takes the generic form

$$\pi_{r,\varphi} = -\chi_\varphi\,\mathrm{d}U_\varphi/\mathrm{d}r + V_{\mathrm{pinch}}U_\varphi + \pi_{\mathrm{resid}}, \tag{1}$$

where π_{resid} is the residual stress driven by the pressure gradient ∇P_{i}, which saturates with increasing ∇P_{i}. The calculation of

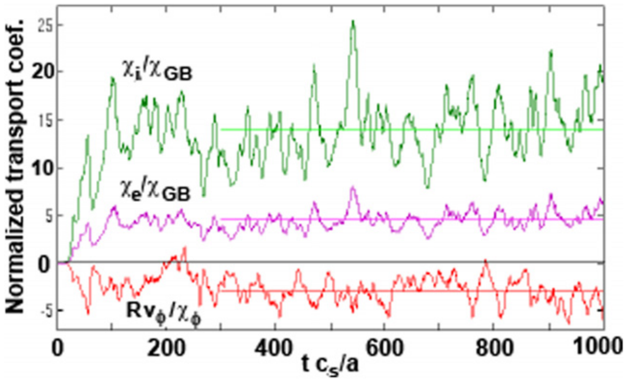

Figure 6. Time behaviour of normalized ion and electron heat diffusivities χ_i/χ_{GB} and χ_e/χ_{GB} and normalized pinch velocity Rv_ϕ/χ_ϕ.

the TEP (turbulent equipartition) and thermoelectric pinches of toroidal momentum and their implication for the rotation profile evolution are also provided. The origin of the spontaneous rotation is discussed in the following several reports. Aydemir shows that the intrinsic angular momentum source arises, when the up–down symmetry is removed [8]. Calculations with the CTD code show very good qualitative agreement with 'transport-driven' flows measured on the C-Mod tokamak. Callen *et al* discuss the influence of toroidal non-axisymmetry effects on plasma rotation [9]. It is shown that such effects can excite the intrinsic rotation also. Honda *et al* consider another origin of the spontaneous rotation [10]. It is shown that the fast particles (which appear at the NBI or ICRH heating) can excite the charge separation and radial currents, which generate torque and, as a consequence, spontaneous rotation.

Peeters *et al* investigate the problem of the momentum pinch [11]. The calculations are performed with the gyro kinetic code GKW, which uses the flux tube geometry. The diffusive part of momentum transport χ_φ is investigated. It is found that the Prandtl number Pr is limited in the range $Pr = \chi_\varphi/\chi_i = 0.7 - 1.2$, where χ_i is the ion heat diffusivity. Figure 6 shows the time behaviour of several calculated values: normalized ion and electron heat diffusivities χ_i/χ_{GB} and χ_e/χ_{GB}, and the normalized momentum pinch velocity Rv_ϕ/χ_ϕ. The value of v_ϕ is negative, i.e. directed inwards. Bateman *et al* report about simulation of the momentum transport [12]. The quasi-linear transport code GLF23 together with the code PEDESTAL is used. Figure 7 shows the comparison of the calculated profiles with the experimental data for a particular JET discharge.

2.3. Plasma heating

Several reports consider the changes in transport at the additional plasma heating. Ishizawa *et al* investigate the turbulent transport by a reduced set of two-fluid 3D equations [13]. Self-consistent calculations of interactions among electro-magnetic micro-turbulence, zonal flows and macro-MHD instabilities are given, and fast turbulent thermal diffusion found in a regime of strong external heating. Some results of the calculations are shown in

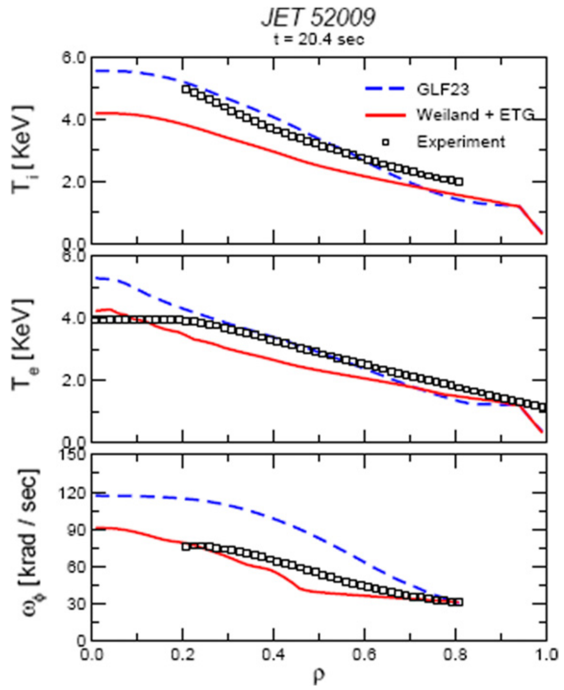

Figure 7. Experimental and calculated by different models ion temperature (top), electron temperature (middle) and toroidal angular rotation frequency (bottom) as a function of normalized minor radius for JET shot #52009.

figure 8. It is shown that inside the plasma region, where the heat flux rises, the heat diffusivity coefficients also increase. The relatively small increase in the temperature gradient leads to heat diffusivity increase of several times.

Pastukhov *et al* present the modified version of 2D code CONTRA-C based on the adiabatically reduced one-fluid MHD, which was used in the simulations for T-10 conditions [14]. The following example is considered (figure 9): initially all electron cyclotron (EC) power is deposited at $r = 12$ cm. Then (at $t = 25$) part of the power (up to 70%) is shifted to the point $r = 25$ cm. The evolution of anomalous factor in the heat flux Fa $= q_{total}/q_{neo}$ is calculated. It is seen that after the decrease in the deposited power at the point $r = 12$ cm, the anomalous factor at the points $r = 13$ and 20 cm diminishes down to the neoclassical level. At the same time the anomalous factor at the point $r = 27$ cm remains high. The dimensionless time unit corresponds approximately to 60 μs for T-10 conditions. The described picture corresponds to the experiments with off-axis ECRH heating. After switch-on of the gyrotron the electron heat diffusivity in the plasma core diminishes but at the plasma periphery (outside the ECRH region) this diffusivity rises.

2.4. Other transport problems

Del-Castillo-Negrete *et al* report about the 1D model of the perturbative non-local transport, which is applied to the edge cold pulse problem [15]. The heat flux here is defined by the fractional-diffusion operator:

$$q_{nl} = -\chi n[l_a D_x^{\alpha-1} - r_x D_b^{\alpha-1}]T, \tag{2}$$

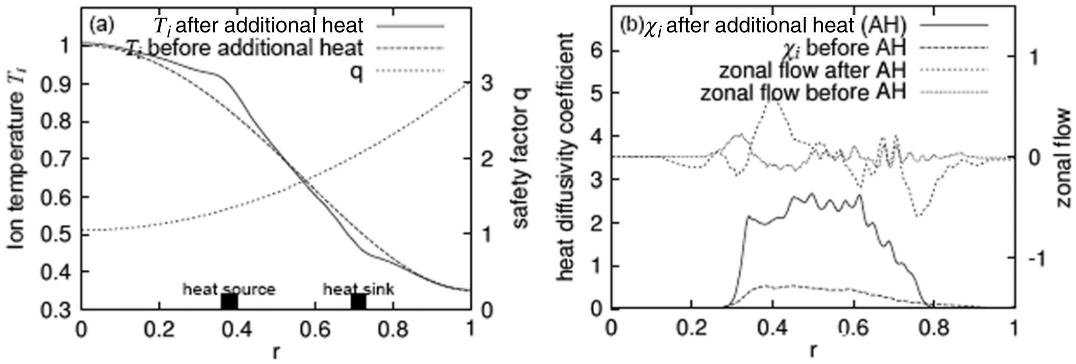

Figure 8. (*a*) The steepening of ion temperature profile T_i by additional heating. (*b*) The thermal diffusivity coefficient inside the high heat flux region increases by a factor of 4–5.

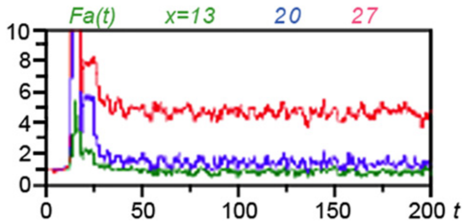

Figure 9. Evolution of anomalous factor of flux Fa $= q_{\text{total}}/q_{\text{neo}}$ at three radial positions: $r = 13$ cm (lower, green), $r = 20$ cm (middle, blue), $r = 27$ cm (upper, red). The dimensionless time unit corresponds to $\sim 60\,\mu$s for T-10.

where ${}_aD_x^{\alpha-1}$ and ${}_xD_b^{\alpha-1}$ are the integro-differential operators defined as

$$
{}_aD_x^{\alpha-1}T = \frac{\partial}{\partial x}\left(\int_a^x \frac{T(y,t)}{(x-y)^{\alpha-1}}\,\mathrm{d}y\right),
$$

$$
{}_xD_b^{\alpha-1}T = -\frac{\partial}{\partial x}\left(\int_x^b \frac{T(y,t)}{(y-x)^{\alpha-1}}\,\mathrm{d}y\right) \qquad (3)
$$

At $\alpha \to 1$, this operator is close to convection, at $\alpha \to 2$ it is close to diffusion. Figure 10 shows the inward propagation of the cold pulse generated at the point $x = 0.75$ for the typical JET discharge. Three different values of parameter α ($\alpha = 1.25$, 1.75 and 1.99) are used in the calculations. It is seen that for lower values of α the time delay of the cold pulse in the plasma centre is of order 5 ms, that is close to the experimental results. To date, the Del-Castillo-Negrete model offers the best fit to the measured time delay.

The report by Dnestrovskij *et al* [16] presents the critical gradient transport model, where the critical gradients are based on the variation principle of magnetic energy minimum. The non-linear version of the canonical profiles transport model (CPTM) includes both the heat and particle fluxes, and also describes the external thermal barrier (ETB). The model does not contain free parameters. It was applied to the simulation of core and pedestal plasma in JET and MAST ELMy and ELM-free H-mode shots. Figure 11 shows the RMS deviations of the calculated profiles from the experimental ones for several plasma discharges. This figure characterizes the quality of simulations. Note that the CPTM has no equation for the momentum transport so far.

Angioni *et al* report about the gyrokinetic simulations of impurity, He ash and alpha-particle transport [17]. Linear and non-linear simulations with three gyrokinetic codes, GS2, GYRO and the recently developed GKW, are performed in concert with the analytical derivations in order to elucidate the basic transport mechanisms of impurities and energetic α-particles. In addition, the ASTRA transport code and the GLF23 model are applied to the modelling of the ITER standard scenario, in which the transport of minority species is included by means of formulae, which fit the gyrokinetic results. Some interesting results of the calculations are illustrated by figure 12. It is seen that while the density of He in the vicinity of the plasma centre is practically the same for different concentrations of He (*a*), the peaking of the He profile diminishes sharply with the rise of average He concentration (*b*).

Heikkinen *et al* present the global gyrokinetic full f particle-in-cell code ELMFIRE, used for transport simulation in tokamaks [18]. ELMFIRE is benchmarked on the small FT-2 tokamak. Figure 13 shows the comparison of the calculated poloidal velocity with the same value measured by reflectometry in FT-2. Reasonable agreement is seen. Catto *et al* propose a fresh idea, namely how to improve the gyrokinetic codes [19]. In contrast to the typical gyrokinetic treatments, canonical angular momentum is taken as the gyrokinetic radial variable rather than the radial guiding centre location. Such an approach allows strong radial plasma gradients to be treated. The non-linear gyrokinetic equation obtained is capable of handling such problems as orbit squeezing effects on zonal flow, collisional zonal flow damping, as well as the neoclassical transport in the pedestal or ITB.

3. Waves and instabilities

A number of reports focused on disruption physics and analysed the detailed path to disruption. These paths included growth and saturation of magnetic islands, the mitigation of ELMs, the suppression of sawteeth and the stabilization of resistive wall modes (RWMs).

3.1. Magnetic islands

Wilson *et al* consider the interaction between transport and reconnection processes [20]. The distribution function in the vicinity of the island separatrix taking account of the

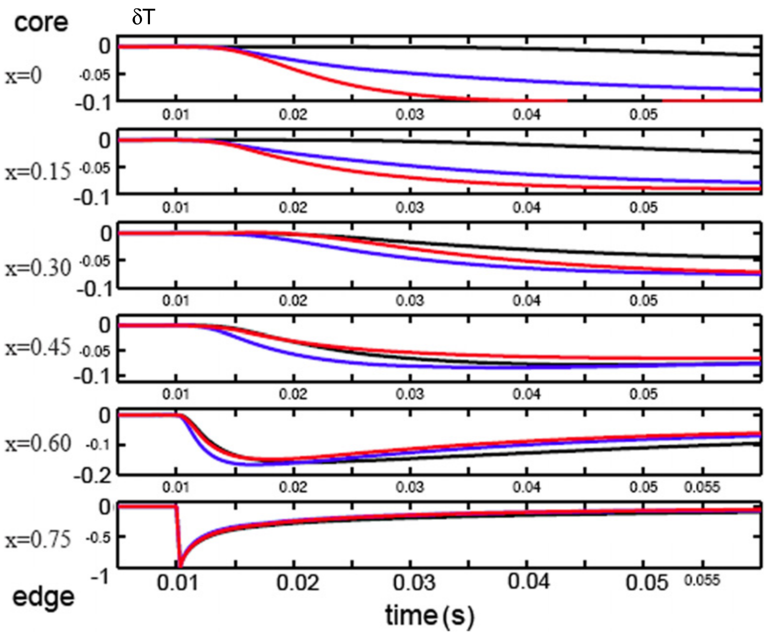

Figure 10. The calculated temperature cold pulse propagation with initial location at the point $x = 0.75$ and $\alpha = 1.25$ (red), 1.75 (blue) and 1.99 (black)

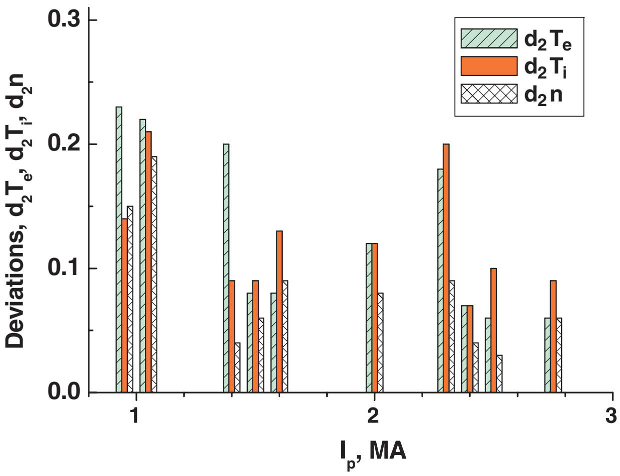

Figure 11. The RMS deviations of the calculated profiles from the experimental ones for electron and ion temperatures and plasma density for 10 JET ELMy H-mode shots.

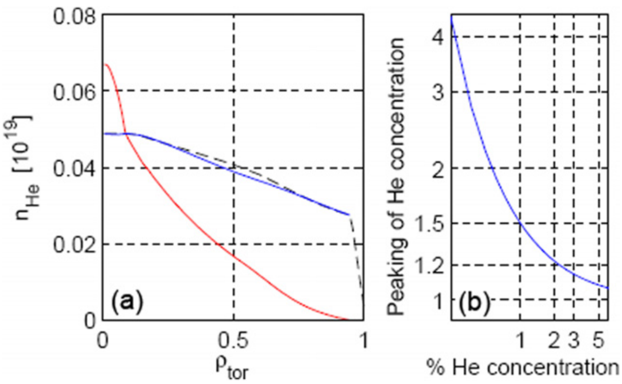

Figure 12. He profiles (a) and peaking of the He profile as a function of the total He concentration (b) of ASTRA-GLF23 ITER simulations.

competition between parallel (to field lines) and perpendicular transport was evaluated numerically. A little further from the island separatrix, collisions play an important role in matching the region, where the distribution function becomes Maxwellian, that is constant on the perturbed flux surfaces of the magnetic island. A full form for the distribution function in three regions, the island separatrix layer, an intermediate collisional layer and a region dominated by parallel transport, is derived. The profiles of the electrostatic potential calculated with the found distribution function are shown in figure 14. These results allow one to find the impact of the cross-field transport on the polarization current (right-hand-side part in the Rutherford equation for island width).

Furukawa *et al* develop the theory for error-field-induced magnetic islands taking into account the Alfvén resonance effect for rotating plasmas in the circular cylinder model [21]. Such a problem arises with application of the resonant magnetic perturbations (RMPs). Only the case with the separation of the twin Alfvén resonances being larger than the island width is considered. The Alfvén singularity in the linear equation for perturbations is avoided by the addition of the imaginary part to the Alfvén frequency. The system of equations concerning the amplitudes is solved numerically. Figure 15 shows the dependence of island width on the error field parameter $|\psi_{err}|$, which is proportional to the jump of the tangential component of the magnetic field across the error-field-coil layer outside the conductive wall. In the figure ‘w/ A.r. (w/o A.r.)’ denotes data with (without) the Alfvén resonances. Without the Alfvén resonance, the island of width $w = 10^{-2}$ can be generated by $|\psi_{err}|$ of order 10^{-3}. On the other hand, when the Alfvén resonance effect is included, significantly large $|\psi_{err}|$ is needed to generate the islands. Figure 15 also shows the scaling change due to the inclusion of the Alfvén resonances.

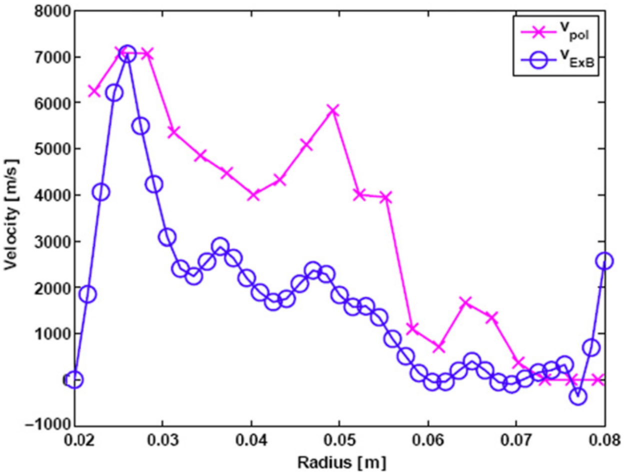

Figure 13. The simulated $E_r \times B$ velocity (blue circles) and total poloidal velocity of fluctuations in FT-2 (violet crosses) measured by reflectometry.

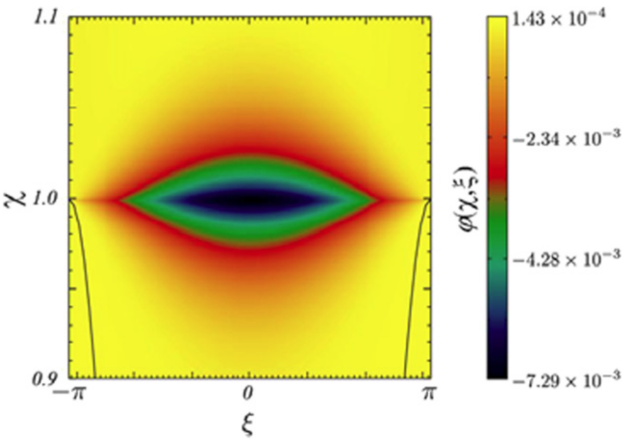

Figure 14. 2D colour contour plots of the electrostatic potential in the vicinity of the island separatrix ($\chi = 1$). The coordinates χ and ξ are the radial and toroidal ones beyond the island.

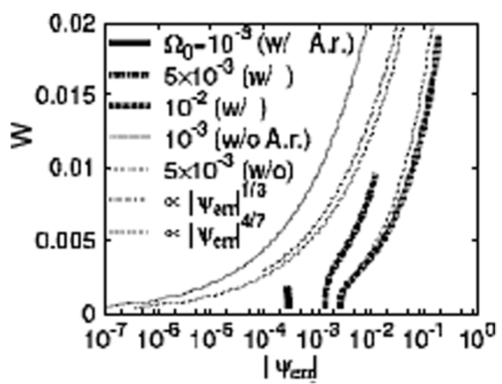

Figure 15. Island width as a function of error field with and without Alfvén resonance effect.

3.2. ELMs and sawtooth

Becoulet *et al* investigate the penetration of RMPs into a plasma [22]. The non-linear cylindrical reduced MHD code is used to describe the process of penetration taking into account the plasma rotation. The typical structure of the magnetic field

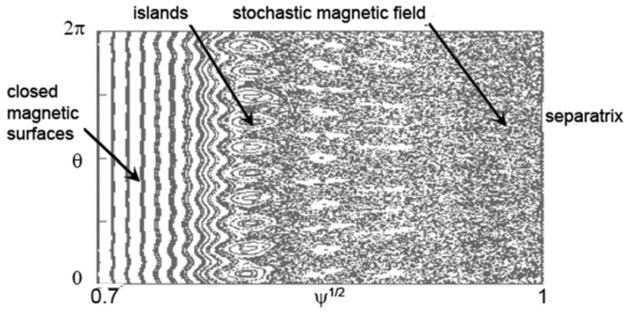

Figure 16. The structure of the magnetic field in the vicinity of the separatrix.

in the vicinity of the separatrix is shown in figure 16. We see the region with stochastic magnetic field, the region filled by islands and finally the region with closed magnetic surfaces. The ELMs amplitudes are suppressed by the existence of the stochastic magnetic field layer. Several conclusions are drawn: (i) the shielding of the RMP is larger for stronger rotation, but (ii) the plasma rotation brakes by the RMP and can even be stopped; (iii) periphery density transport rises with the RMP. Note that the braking of the plasma rotation increases the danger of disruption. The same problem of the influence of the RMP rotation on plasma transport is considered by Strauss *et al* [23], who used the M3D code. Figure 17 illustrates one of the obtained results: it shows the temperature profiles with RMP, but without rotation (a), while (b) corresponds to rotation and RMP. It is seen that in spite of RMP persistence, the account of rotation expands the region of hot plasma and improves the energy confinement. Unfortunately, this conclusion is not confirmed by the experiment so far.

The problem of thermal diffusion in destroyed magnetic field is considered by Hudson *et al* [24]. This problem is connected with the RMP impact on confinement discussed in the Becoulet *et al* report [22]. A chaotic magnetic field is a fractal mix of (i) invariant flux (KAM) surfaces, which are labelled by their irrational rotational transform; (ii) Cantori (broken KAM surfaces), in particular the near-critical Cantori, which present effective but partial barriers to field-line transport; (iii) unstable periodic orbits, which constitute the stochastic sea; (iv) stable periodic orbits and elliptic island chains. Cantori are approximated by high-order, action-minimizing periodic orbits. It is also proposed that $k_\perp/k_\parallel \sim 10^{-10} \ll 1$, where $k_\perp$ and $k_\parallel$ are perpendicular and parallel heat diffusivities. The coordinate system connected with the magnetic field structure is constructed. The magnetic field lines are stationary curves of the action integral $S_C = \int_C \boldsymbol{A}\,\mathrm{d}\boldsymbol{l}$, where $\boldsymbol{A}$ is a vector potential. The Euler–Lagrange equations in this case have the form of Hamilton's equations. A special role is played by the 'ghost' surfaces, which are constructed by pushing a trial curve off the minimax orbits. These ghost surfaces are defined using the action-gradient flow. Any selection of ghost surfaces may form the framework of chaotic coordinates. The authors say 'intuition suggests the irrational ghost-surfaces would coincide with temperature iso-contours'. The heat diffusivity equation is solved numerically using the constructed coordinate system. The magnetic field is perturbed by 2/1 and 3/2 harmonics, and the region between two magnetic islands, $m/n = 2/1$ and $3/2$ ($\psi = 1/2$ and

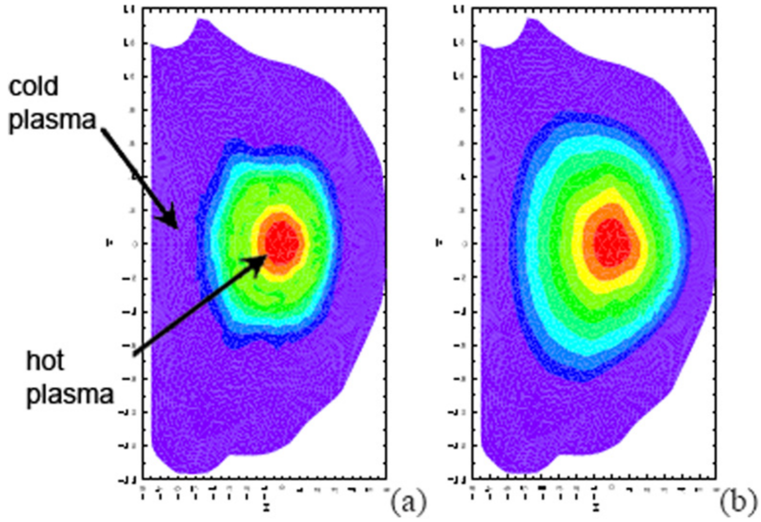

Figure 17. (*a*) DIII-D plasma isotherms with RMP, but without toroidal rotation. (*b*) Plasma isotherms with RMP and with toroidal rotation.

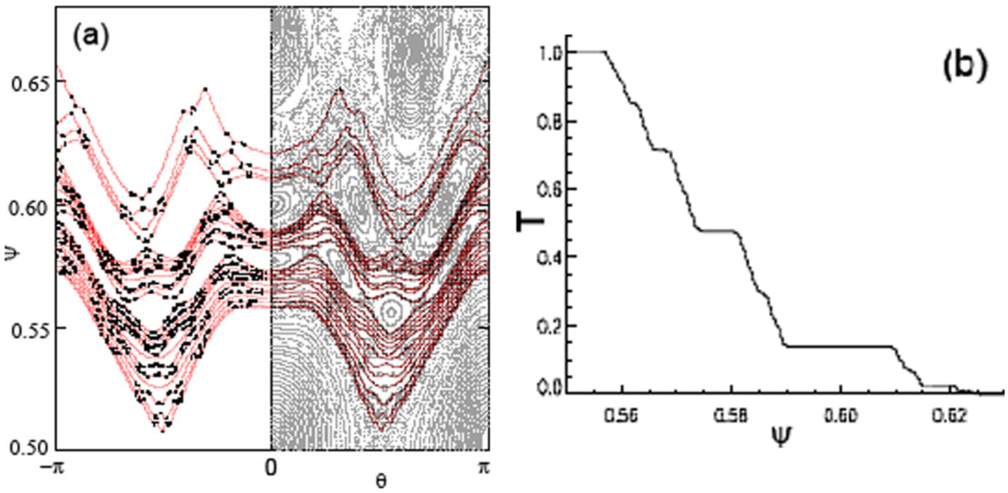

Figure 18. (*a*) Left side: the selected ghost curves (red lines) and Cantori (black square dots); right side: Poincaré plot (grey dots), ghost curves (red lines) and the temperature contours (black lines). (*b*) Temperature profile along the line $\theta = 0$.

2/3, respectively), is considered. The left half of figure 18(*a*) shows the selected ghost curves and Cantori. It is seen that at $\psi \sim 0.55$ the KAM surfaces are just destroyed, the Cantori are close to each other and they are lying over the ghost curves. In contrast, at $\psi \sim 0.6$, the KAM surfaces are strongly destroyed and the Cantori are sparse. The ghost curves and isotherms, shown in the right part of figure 18(*a*), are hardly distinguished. The temperature profile along the symmetry line $\theta = 0$ is shown in figure 18(*b*).

Hayashi *et al* present the results of the integrated simulation of ELM energy loss and cycle in the H-mode plasma [25]. The stability code MARG2D for peeling–ballooning modes is used with the transport model of the scrape-off layer (SOL) and divertor plasma. It allows them to track the plasma evolution during several ELMs periods. Figure 19 shows some of the obtained results. At the moment when the steep gradient inside the ETB becomes unstable, the heat diffusivity in the ETB increases artificially up to $100\,\mathrm{m^2\,s^{-1}}$ over a time interval of $200\,\mu\mathrm{s}$ (figure 19(*b*)). The electron temperature profile changes (figure 19(*a*)), and part of the energy storage is rejected from the plasma. Then the restoration of the temperature profile begins. The time behaviour of the energy storage for different values of the deposited power is shown in figure 19(*c*). It is seen that the period of ELMs diminishes with an increase in the deposited power. Chapman *et al* consider the physics of sawtooth (ST) stabilization [26]. The JET discharge #58855 is discussed. First the on-axis NBI is switched on and the period of ST during this stage is large (figure 20). Then the off-axis NBI is switched on, and the power of on-axis heating diminishes simultaneously. It is seen that the ST period shortened sharply. This effect is explained by the destabilizing contribution from passing fast ions born outside $q = 1$ at the off-axis NBI heating.

3.3. *Stability of RWM*

Liu *et al* discuss the stability of RWMs influenced by drift kinetic resonances [27]. The kinetic terms are included self-consistently in the MHD equations. Figure 21 illustrates some results. Here the dependence of the variation of potential energy δW is shown versus the ratio r_w/a, where r_w is the wall radius and a is the plasma minor radius. Note that in

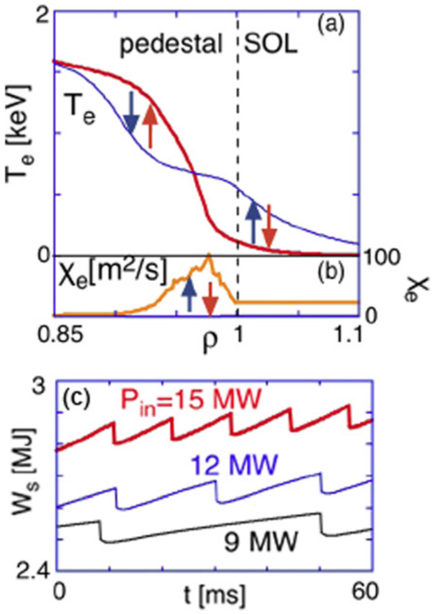

Figure 19. (*a*) Profiles of electron temperature just before and after ELM in JT-60U; (*b*) heat diffusivity during ELM; (*c*) time evolution of stored energy W_s for net input powers of $P_{\mathrm{in}} = 9$, 12, 15 MW.

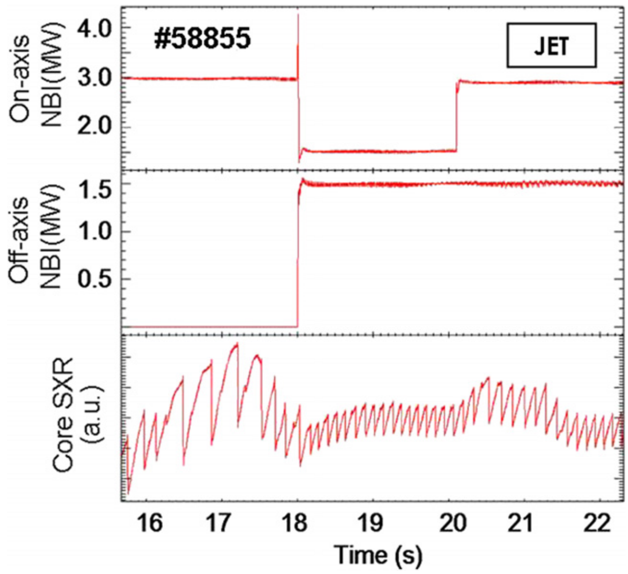

Figure 20. Time behaviour of SXR signal at the on-axis NBI ($t < 18$ s) and at the off-axis NBI ($18 < t < 20$ s).

the case $\delta W > 0$ (<0) the RWMs are stable (unstable). If the wall is absent (red solid line) the RWMs are unstable. In pure MHD approximation (red dashed line), the approach of the wall to the plasma surface improves the stability of the RWM. But if the kinetic terms are taken into account, the RWMs become unstable, when the wall approaches the plasma (blue solid line). This happened due to the modification of the eigenmode structure of the RWM in this case.

3.4. Plasma heating and current drive

Vdovin analyses plasma heating and current drive by the EC and ion cyclotron (IC) waves [28] using the 3D code STELEC.

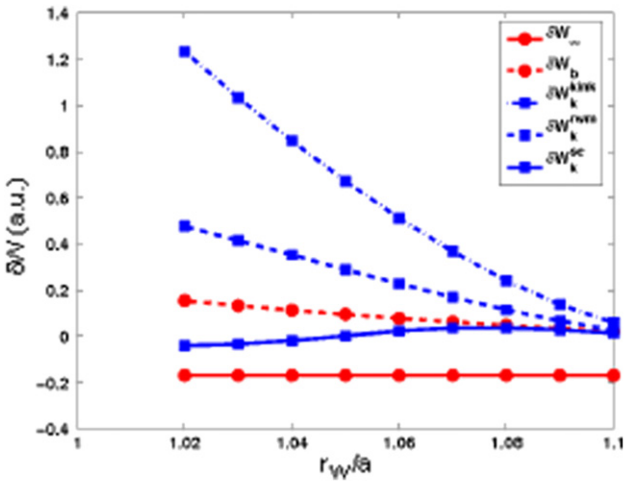

Figure 21. The radial variation of the potential energy for different plasma models: no-wall ideal MHD (red solid line with circles), pure MHD model (red dashed line with circles) and MHD model with kinetic terms (blue solid line with squares).

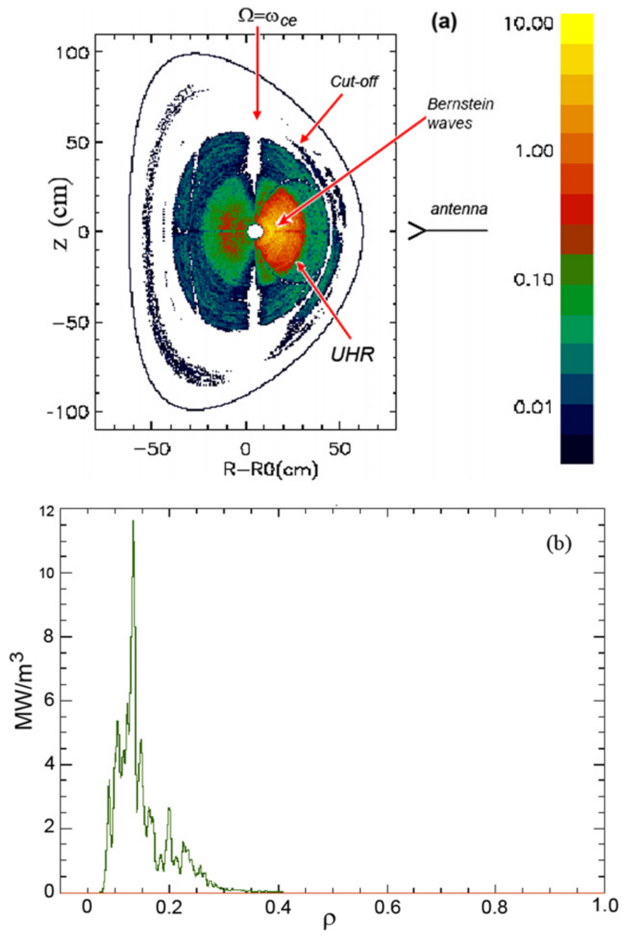

Figure 22. Absorption of EC waves over the plasma cross-section (*a*); fine structure on the power deposition function is evidence of EBW (*b*).

The results of modelling for the NSTX tokamak are shown in figure 22. For this particular example, the O-mode at the fundamental EC frequency perpendicular to the plasma boundary is injected (*a*). In toroidal plasma the O- and X-modes are coupled, so the main part of wave energy is

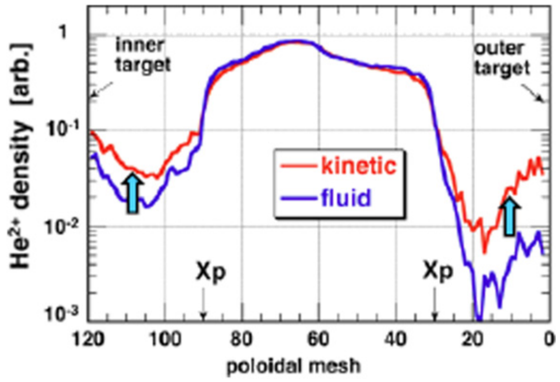

Figure 23. He^{2+} density profile in the flux tube close to the separatrix surface. Blue (lower) and red (upper) lines relate to fluid and kinetic models correspondingly.

absorbed in the vicinity of the upper hybrid resonance (UHR) by the electron Bernstein wave (EBW) branch. It is seen (*b*) that the waves are absorbed before they come to cyclotron resonance.

4. SOL

Shimizu *et al* consider the kinetic modelling of impurity transport in SOL [29]. The Monte Carlo impurity code IMPMC connected with the divertor code SOLDOR/NEUT2D is used. The calculations are compared with the results obtained by conventional (fluid) evaluations. Figure 23 illustrates the provided comparison. Here the helium density in the SOL is shown to be obtained by the new kinetic model (red (upper) line) and by the fluid model (blue (lower) line). Note that the logarithmic scale in the vertical direction is used. It is seen that behind the separatrix in the vicinity of the equatorial plane, the kinetic results exceed the fluid ones by factors of 2–6. This effect can improve the conditions of helium pump-out from the divertor region. Takizuka *et al* report about the flow pattern inside the SOL [30]. A two-dimensional full particle simulation code PARASOL is used. The situation with upper and lower x-points (UN and LN cases) is considered carefully. The comparison of the calculated data with the experiment in Alcator C-Mod is shown in figure 24. The qualitative correspondence between calculations and experiment is well seen. In the inner SOL the signs of the parallel velocities $V_\parallel$ are different in the UN and LN cases. In the outer SOL the signs of $V_\parallel$ are the same.

5. ITER

Pacher *et al* calculate the ITER operation window in ELMy H-mode at 15 MA [31]. Modelling is carried out with the 1.5D ASTRA code, in which the Integrated Core Pedestal SOL (ICPS) model has been implemented. Figure 25 shows the results of calculations on (P_{alpha}, Q) plane. Here P_{alpha} is the power (in MW) in α-particles and Q is the ratio of fusion power to the external deposited power. The ITER planning operation point, marked by a cross, is placed in the operation window (shaded/yellow-green). These calculations show that the ITER has some reserve relative to the planning value of $Q = 10$. The possibility to work with $Q = 20$ means that the deposited power can be diminished twice, i.e. from 50 MW to 25 MW.

6. Stellarators and other helical configurations

The nature of energy and particle transport in stellarators remains uncertain. On the one hand the neoclassical transport is high and for the most part can describe experiments. On the other, there exist some phenomena (H-mode, ITBs, energy confinement time scaling) that confirm the turbulent nature of plasma transport. In this section we consider the reports devoted to these problems: role of neoclassical transport, turbulent transport and self-consistency of pressure profiles in stellarators. The difficulties connected with the construction of 3D MHD solutions are also considered.

Beidler *et al* discuss the role of neoclassical transport in stellarators [32]. The goal of this collaborative report is to provide a comprehensive description of neoclassical transport processes in stellarator experiments. The approach consists of benchmarking various numerical methods used to calculate the mono-energetic neoclassical transport coefficients in 3D magnetic field topology with multiple classes of trapped particles. Many conclusions are made in this paper, so we mark only the following ones:

i. All devices exhibit radial transport in the long-mean-free-path regime, which scales as $1/\nu$ with the collision frequency.
ii. This $1/\nu$ transport can be partially suppressed by the radial electric field E_r.
iii. For the radial transport of particles and heat, the effects of momentum conservation are entirely negligible.

Watanabe *et al* discuss the importance of turbulent transport in stellarators [33]. The gyrokinetic Vlasov simulations are performed by using the GKV code in application to the Large Helical Device (LHD). In this device improved confinement occurs when the magnetic axis is shifted inwards (major radius diminishes). The simulation result obtained for the inward-shifted LHD configuration shows generation of large amplitude stationary zonal flow structures leading to significant turbulent transport reduction. This provides a possible explanation for the observed improvement of confinement. Figure 26 shows the time behaviour of the calculated normalized ion heat diffusivities for standard and inward-shifted LHD magnetic configurations. It is seen that calculations really predict the improved confinement for the inward-shifted configuration.

Dnestrovskij *et al* consider the problem of self-consistency of pressure profiles in stellarators [34]. The electron plasma pressure, p_e, presents strong profile resilience in the confinement zone of the plasma column in TJ-II (figure 27). To describe the pressure self-consistency, the authors use the variation problem to minimize the energy functional W under the constraint that the total plasma current J is fixed. The solutions of the Euler equation are called canonical profiles. The general equilibrium equation for the canonical profiles is obtained. In the cylindrical low-β approximation the canonical pressure profiles have the following form:

$$p_c(\xi) = p_0 \exp\left\{ -2\left[\ln\left(\frac{p_0}{p_b}\right) \Big/ \left(1 + \frac{\mu_b}{\mu_0}\right)\right] \times \rho^2 \left[1 + \left(\frac{\mu_b}{\mu_0} - 1\right)\rho^2/2\right]\right\}, \tag{4}$$

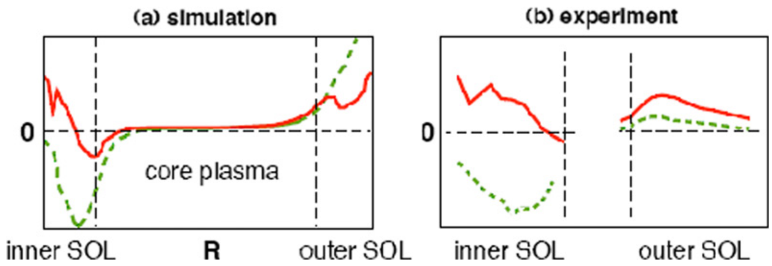

Figure 24. Radial profiles of parallel velocity $V_{\parallel}$ in the SOL for upper null (UN) configuration (dashed green line) and lower null (LN) configuration (solid red line) for simulation (*a*) and the experiment in Alcator C-Mod (*b*). The direction of toroidal drift is fixed.

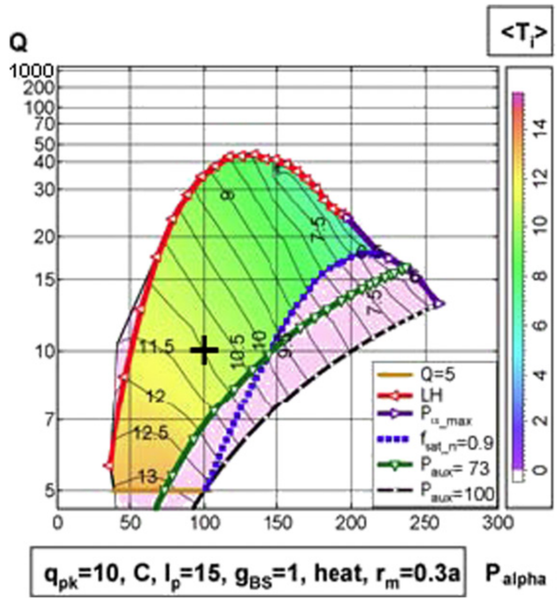

Figure 25. The operation window for ITER discharges in ELMy H-mode at a plasma current of 15 MA. The planning point is marked by a cross.

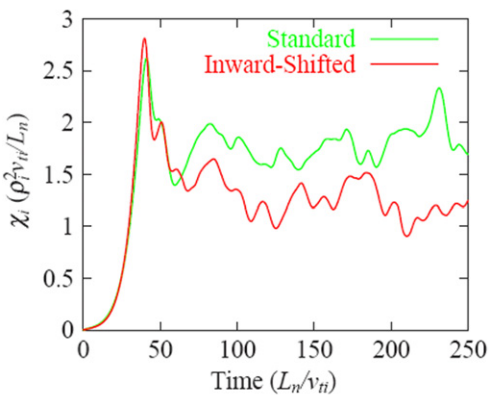

Figure 26. Time history of the ion heat conductivity χ_i for the inward-shifted (lower curve) and standard (upper curve) LHD configurations.

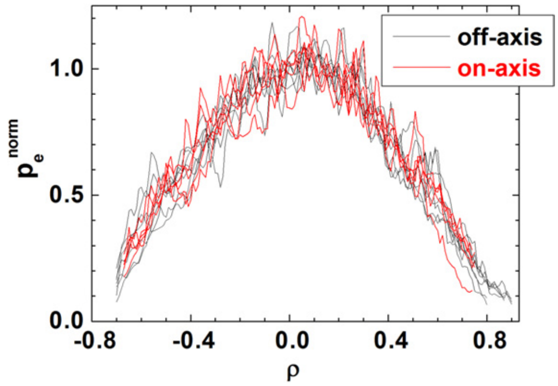

Figure 27. The normalized pressure profiles in TJ-II are well conserved in discharges with on-axis and off-axis EC heating and NBI heating.

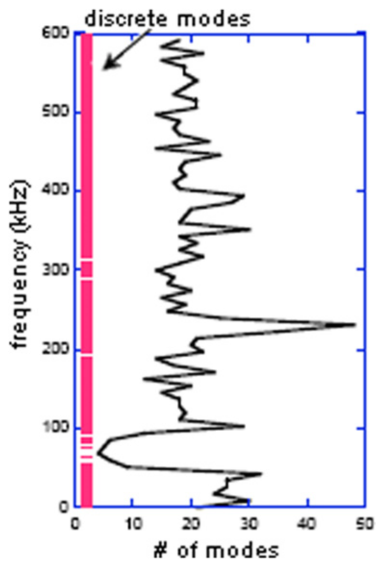

Figure 28. Alfvén eigenmode density versus frequency.

where p_0 and p_b, μ_0 and μ_b are the central and boundary values of pressure and rotational transform correspondingly, $\rho = r/a$ is the dimensionless radial coordinate.

The existence and stability of shear Alfvén (SA) modes in stellarators were examined computationally by Spong *et al* [35] through a sequence of continuum, discrete eigenmodes and δf calculations. Both regimes with benign effect on fast particle confinement have been seen in the experiment, as well as those with enhanced losses. Although 3D couplings greatly increase the number of available SA modes, many of these are continuum damped. In order to better interpret the experimental results, the numerical methods were developed to calculate the Alfvén continuum (STELLGAP code) and discrete mode structure (AE3D code, reduced MHD) taking into account the 3D equilibrium. In figure 28 the results from the AE3D code are shown for the LHD discharge #47645 for hydrogen plasma with a density $\bar{n} = 1 \times 10^{20}\,\mathrm{m}^{-3}$. This figure shows the density of modes versus frequency. Here the $n = 1$ mode family was coupled with $n = -11, -9, -1$, 9 and 11 modes. The low-energy modes are of most interest. We see that clumps of low-energy modes present at frequencies corresponding to the more open continuum gap regions near the 50–60 kHz range. A new method for evaluating the stability of these modes has been developed as an extension to the AE3D calculations. This is done in the time domain using the δf method. Stability and linear growth rates can be assessed from the ensemble-averaged wave–particle energy transfer data.

Hole *et al* develop a model for the mathematically rigorous description of equilibria in fully 3D geometry [36]. The model consists of a stepped pressure profile, where the steps correspond to the ideal MHD barriers across which can be supported a pressure or field jump, or a jump in rotational transform. In the 3D case it is envisaged that the barriers can be chosen to be non-resonant KAM surfaces that survive the onset of field-line chaos intrinsic to the 3D equilibrium. In between the interfaces, the field is Beltrami, such that $\nabla \times \boldsymbol{B} = \mu \boldsymbol{B}$. The boundary condition across the interfaces is the continuity of the total pressure $p + B^2/2\mu_0$. For the solution of such a problem the variation principle of the minimum of total energy W is used, where $W = \int \mathrm{d}V(B^2/2 + p/(\gamma - 1))$, under constraints provided by ideal MHD (conservation of global poloidal and toroidal magnetic fluxes and global helicity). As a result, the system of equations for the perturbation coefficients and the linear eigenvalue equation for λ is obtained. In parallel, more standard tearing mode treatment is developed. Both problems are solved as an example for FRP-like configuration in a circular cylinder plasma approximation. It is shown that the marginal stability conclusions of the two models are identical.

7. Fast particles

Despite advances, the confinement of alpha-particles in reactor environments and ITER remains uncertain. While neoclassical diffusion and diffusion due to turbulence generated by drift instabilities do not cause substantial confinement loss, diffusion due to Alfvénic instabilities driven by hot particles themselves could be substantial.

Chen *et al* present the gyrokinetic simulation of energetic particle turbulence [37]. The GTC and GYRO codes are used. It is shown that the energetic particle transport induced by the ITG micro-turbulence decreases rapidly with the energy rise. In these conditions the diffusion of α-particles will be very slow. Figure 29 illustrates such a conclusion. Here the dependence of the normalized fast particle diffusivity is shown versus the ratio E/T_e, where E is the particle energy and T_e is the electron temperature. For α-particles in ITER, the ratio E/T_e equals 200–300. In these conditions the diffusion of α-particles will be very slow.

Gorelenkov *et al* present a new theory of two classes of energetic particle driven instabilities [38]. The former is a new class of global MHD solutions resulting from the coupling of the Alfvénic and acoustic fundamental MHD oscillations due to geodesic curvature. These modes, called beta-induced

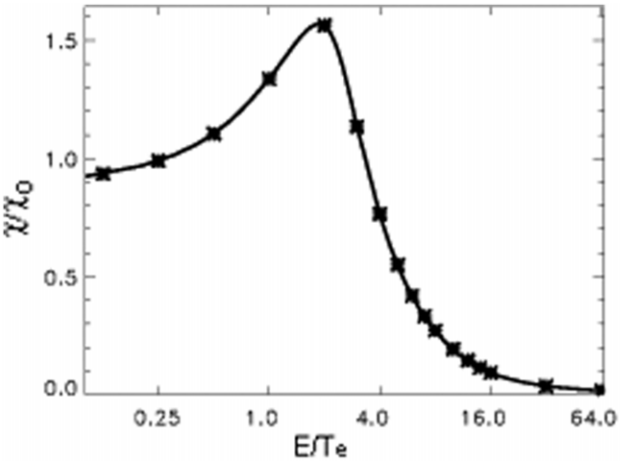

Figure 29. Diffusivity of α-particles driven by the micro-turbulence as a function of the energy for the isotropic, mono-energetic particles model.

Alfvén-acoustic eigenmodes (BAAEs), have been recently observed in several devices. The latter class is the instability of reversed shear Alfvénic eigenmodes (RSAEs), which can be suppressed by a strong magnetic pressure plasma. A kinetic theory is required, if the modes strongly interact with the Alfvén continuum. Figure 30 shows the schematic of the Alfvénic and acoustic continuum in a cylinder (left figure) and in a torus (right figure). In the case of the torus, instead of lines intersections we can observe frequency gaps, which means the appearance of instabilities. Three gaps are seen in the figure. The upper gap corresponds to very known toroidal Alfvén eigenmodes (TAEs). The next one relates to RSAE and beta-induced Alfvén eigenmode (BAE). The lower gap corresponds to the BAAE mode. The beta effects on two solutions, RSAE and BAAE, in the NSTX conditions are the subject of this work. It is shown that due to large plasma beta in NSTX, characteristic frequency sweeping of RSAEs is suppressed. These modes are often stabilized by the finite pressure. New low frequency modes exist in the BAAE gap with the frequency below GAM. BAAEs induce losses of beam ions and form avalanches in NSTX. The kinetic theory of BAAEs is formulated.

8. Conclusions

1. In this Conference the most attention was attracted to the research on transport processes. A characteristic feature was higher interest in toroidal momentum transport.
2. The gyrokinetic codes are extended over the world. The number of codes exceeds two dozen. Both the development of computers and elaboration of the improved difference schemes are going simultaneously. The achieved time interval for plasma simulations has now reached times comparable to the ion–ion collision time. However, the real perspective to describe transport in ITER is the combination of the gyrokinetic and fluid codes.
3. Theoretical analysis and calculations show that the RMPs, mitigating the ELMs, could brake the plasma rotation, increasing the danger of disruption. Indeed, ELM

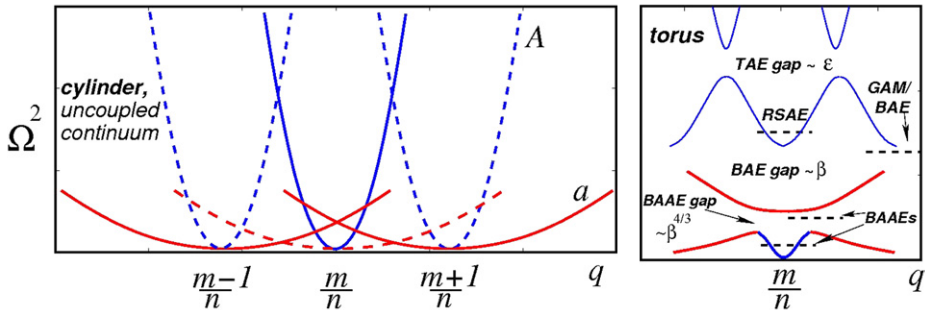

Figure 30. Schematic of the Alfvénic and acoustic continuum in a cylinder (left) and in a torus (right). 'A' and 'a' correspond to the Alfvén and acoustic modes. The gaps correspond to complex roots (unstable or dumping modes).

Table 2. Distribution of theoretical reports among countries.

Country	Number of reports
USA	30
Japan	25
Germany	10
Russian Federation	10
France	7
Italy	6
UK	5
China	4
Republic of Korea	4
Others	37
Total number of reports	128
Total number of countries:	26

suppression by RMPs was a highly topical feature amongst the reported experimental results at the Conference. Hence the lack of complete understanding of the physics of ELM suppression by RMP constitutes an important theoretical challenge en route to ITER.

4. The problems of the SOL and divertor attracted the largest number of theoreticians. The unsolved problem of energy extraction from reactor plasma forced the scientists both to improve the understanding of periphery plasma processes and to suggest new ideas.
5. ITER and reactor problems remain the central focus of attention. ASTRA transport simulation predicts that ITER will operate as expected for $Q = 10$ or larger.
6. Some reports confirm that neoclassical transport dominates in the stellarator. However, the influence of turbulent transport can define such important effects as improved confinement regimes and the resilience of pressure profiles.
7. It is shown that the alpha-particles diffusion due to ITG turbulence will be small in ITER, but the diffusion due to Alfvénic waves turbulence and stochastic magnetic fields remains the critical issue for ITER.
8. International collaboration in plasma theory and modelling is high. The formal distribution of TH section reports among countries is shown in table 2. But really 70 reports were presented by international teams, which included people from different countries. Hence, the international collaboration coefficient is equal to $C_{\rm ic} = 70/128 = 0.55$, which is larger than one half.

Acknowledgments

The author would like to thank the many people who sent him their reports before the Conference. He is also grateful to Dr S. Lysenko who edited this paper.

References

References presented below as papers at this conference are available online at http://www-naweb.iaea.org/napc/physics/FEC/FEC2008/html/index.htm

[1] Staebler G.M. *et al* Testing the trapped gyro-Landau fluid transport model with data from tokamaks and spherical tori Paper TH/P8-42
[2] Casati A. *et al* 2009 *Nucl. Fusion* **49** 085012
[3] Lin Z. *et al* Gyrokinetic turbulence simulation of physics basis for transport modeling Paper TH/P8-41
[4] Holand C. *et al* Validation of gyrokinetic transport simulations using DIII-D core turbulence measurements Paper TH/8-1
[5] Idomura Y. *et al* 2009 Study of ion turbulent transport and profile formations using global gyrokinetic full-f Vlasov simulation *Nucl. Fusion* **49** 065029
[6] Jenko F. *et al* Multi-scale, multi-mode gyrokinetic simulations and implications for transport modelling of tokamaks and optimized stellarators Paper TH/P8-12
[7] Diamond P.H. *et al* 2009 *Nucl. Fusion* **49** 045002
[8] Aydemir A.Y. 2009 An intrinsic source of radial electric field and edge flows in tokamaks *Nucl. Fusion* **49** 065001
[9] Callen J.D. *et al* 2009 *Nucl. Fusion* **49** 085021
[10] Honda M. *et al* 2009 *Nucl. Fusion* **49** 035009
[11] Peeters A.G. *et al* Gyro-kinetic study of toroidal momentum transport Paper TH/P8-33
[12] Bateman G. *et al* Integrated modeling simulations of toroidal momentum transport in tokamaks Paper TH/P8-35
[13] Ishizawa A. and Nakajima N. 2009 *Nucl. Fusion* **49** 055015
[14] Pastukhov V.P. *et al* Reduction of cross-field plasma transport in tokamaks due to power input redistribution and sheared flow profile modification Paper TH/P8-26
[15] Del-Castillo-Negrete D. *et al* Non-local models of perturbative transport: numerical results and application to JET experiments Paper TH/P8-38
[16] Dnestrovskij A.Yu. *et al* Canonical profile transport model for H-mode shots in tokamaks Paper TH/P8-23
[17] Angioni C. *et al* Gyrokinetic simulations of impurity He ash and particle transport and consequences on ITER transport modeling Paper TH/8-3
[18] Heikkinen J.A. *et al* Full f gyrokinetic simulation of tokamak plasma turbulence using ELMFIRE Paper TH/P8-6
[19] Catto P.J. *et al* Limitations insights and improvements to gyrokinetics Paper TH/P8-37
[20] Wilson H.R. *et al* The interaction between transport and reconnection processes Paper TH/P9-27

[21] Furukawa M. and Zheng L.-J. 2009 *Nucl. Fusion* **49** 075018
[22] Becoulet M. *et al* 2009 *Nucl. Fusion* **49** 085011
[23] Strauss H.R. *et al* 2009 *Nucl. Fusion* **49** 055025
[24] Hudson S.R. *et al* Temperature gradients are supported by cantori in chaotic fields Paper TH/3-2
[25] Hayashi N. *et al* Integrated simulation of ELM energy loss and cycle in improved H-mode plasmas Paper TH/P9-14
[26] Chapman I.T. *et al* 2009 *Nucl. Fusion* **49** 035006
[27] Liu Y. *et al* 2009 *Nucl. Fusion* **49** 035004
[28] Vdovin V.L. Critical problems in plasma heating/CD in large fusion devices and ITER Paper TH/3-5
[29] Shimizu K. *et al* 2009 *Nucl. Fusion* **49** 065028
[30] Takizuka T. *et al* 2009 *Nucl. Fusion* **49** 075038
[31] Pacher G.W. *et al* Operation window with mutually consistent core-SOL-divertor conditions in ELMy H-mode: prospects for long pulse operation in ITER and DEMO Paper TH/P4-1
[32] Beidler C.D. *et al* Results from the international collaboration on neoclassical transport in stellarators (ICNTS) Paper TH/P8-10
[33] Watanabe T.-H. *et al* Regulation of turbulent transport in neoclassically optimized helical configurations with radial electric fields Paper TH/P8-20
[34] Dnestrovskij Yu.N. *et al* Approach to canonical pressure profiles in stellarators Paper TH/P8-24
[35] Spong D.A. *et al* Energetic particle physics issues for three-dimensional toroidal configurations Paper TH/3-4
[36] Hole M.J. *et al* 2009 Relaxed MHD states of a multiple region plasma *Nucl. Fusion* **49** 065019
[37] Chen L. *et al* Gyrokinetic simulation of energetic particle turbulence and transport Paper TH/P3-14
[38] Gorelenkov N.N. *et al* Theory and observations of low frequency eigenmodes due to Alfvén acoustic coupling in toroidal fusion plasmas Paper TH/5-2